



Position-dependent neutron detection efficiency loss in ^3He gas proportional counters

Patrick N. Peplowski ^{a,*}, Zachary W. Yokley ^a, Madison Liebel ^a, Shuo Cheng ^a, Richard C. Elphic ^b, Shannon F. Hoogerheide ^c, David J. Lawrence ^a, Jeffrey S. Nico ^c

^a Johns Hopkins Applied Physics Laboratory, Laurel MD 20723, USA

^b NASA Ames Research Center, Moffett Field, CA, 94035-1000, USA

^c National Institute of Standards and Technology, Gaithersburg, MD 20899-8461, USA



ARTICLE INFO

Keywords:

Neutron detection
 ^3He gas proportional counter
 Neutron efficiency

ABSTRACT

The position-dependent neutron detection response of a ^3He gas proportional counter (GPC) was characterized using a collimated (3-mm-wide), monoenergetic (0.05 eV) neutron beam. For neutrons incident on the GPC near the ends of the active region, the neutron capture peak broadens and the position shifts to lower pulse-height channels. This “edge effect” is due to lower gas gain within the decreasing electric field near the end of the active volume. For simple peak-region-summing analyses, the consequence is a loss of events that is equivalent to a 13% reduction in the active area of our GPC. Summing over all events above the triton wall-effect feature significantly reduces this efficiency loss. Whole-sensor illumination measurements simulated with Geant4 required a correction for the edge effect to accurately reproduce the shape and amplitude of the measurements. Once these corrections were applied, the Geant4 models reproduce the whole-sensor count rates to within 10%.

1. Introduction

Helium-3 (^3He) is a common medium for neutron detection due to the high thermal-neutron-absorption cross section (5330 b) of the $^3\text{He}(\text{n},\text{p})\text{t}$ reaction. This reaction produces two easily-measured charged particles, a proton (p) and a triton (t), whose kinetic energies (573 keV and 191 keV, respectively) sum to the Q-value of the reaction (764 keV). During an ideal neutron detection event, the proton and triton lose all of their kinetic energy within the ^3He gas and a characteristic neutron capture peak appears in the energy deposition spectrum at the reaction Q-value, plus the kinetic energy of the neutron (Fig. 1), which is typically much smaller than the Q-value.

Several geometric effects within the GPC determine the final shape of the energy deposition spectrum. Wall-effect events occur when one of the two reaction products reach the wall of the GPC before losing all of their energy within the gas (e.g. [1]). The energy deposited within the wall is not registered by the sensor, leading the wall-effect events to have measured energy deposition that is less than the reaction Q-value. Wall-effect events manifest as a two-plateau structure – one for the proton, one for the triton – with sharp low-energy edges that have an energy equal to the Q-value minus the maximum particle energy (see Fig. 1).

The second geometric effect is the edge effect, which results from a decrease in ionization-induced electron production via gas multipli-

cation. The edge effect occurs within the active volume of the sensor, near the dead regions, where the electric field rapidly changes from its full value to zero. Edge effect measurements have been reported for several ^3He GPCs [2,3], however the effect, and its implications for neutron detection efficiency, are not widely acknowledged by ^3He GPC manufacturers or users.

Helium-3 neutron sensors have been used for decades for space-based applications in planetary science (e.g. [4]) and national security (e.g. [5]). Our research group is developing ^3He -GPC-based neutron detectors for three upcoming planetary science spaceflight missions: the National Aeronautics and Space Administration's (NASA's) Psyche mission to asteroid (16) Psyche [6], the Japanese Aerospace Exploration Agency's (JAXA's) Mars Moon eXploration (MMX) mission to Mars' moon Phobos [7], and NASA's Dragonfly mission to Saturn's moon Titan [8]. For each of these missions, measurements of neutron emissions from the object's surface materials will be used to constrain the chemical composition of the surface. This requires precise knowledge of the energy- and position-dependent neutron detection efficiency of the sensors. This paper reports measurements of the response of five ^3He GPCs, identical to those planned for flight on the Psyche and MMX missions.

* Corresponding author.

E-mail address: Patrick.Peplowski@jhuapl.edu (P.N. Peplowski).

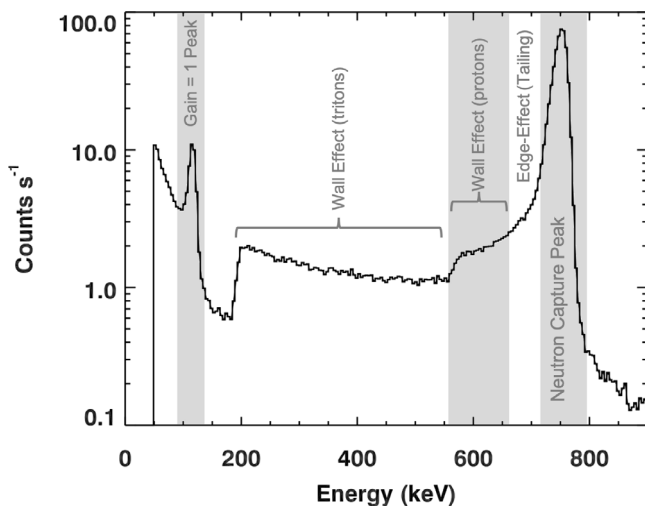


Fig. 1. Annotated ${}^3\text{He}$ spectrum, highlighting neutron capture peak, gain = 1 peak, wall effect, and edge effect.

2. Neutron sensors

The ${}^3\text{He}$ GPCs used for this study were 30.6-cm-long, 5.08-cm-diameter tubes from GE Reuter-Stokes. Fig. 2 details the geometry of the GPCs. The GPCs have a 1.4-mm-thick aluminum housing and are filled with 1013 kPa (10 atm) of ${}^3\text{He}$ gas. The total fill pressure was 1018 kPa, with the difference (5 kPa) being charge and/or UV quenching gas additives that improve the performance of the sensors.

The active volume of the GPC (Fig. 2) represents the portion of the tube for which the gas is within the electric field resulting from

the application of high-voltage bias to the sensor. Events occurring within the active volume are subjected to multiplication of ionization electrons, resulting in increased signal gain. The active length is located between two inactive gas volumes (called dead regions; Fig. 2), which are not within the electric potential when the GPC is under high-voltage bias. Neutron-capture events occurring in the dead regions are not subject to gas multiplication gain, and appear as the gain = 1 peak labeled in Fig. 1.

Two sets of measurements are reported in this paper. The first are profile measurements of the absolute neutron detection efficiency along the length of the tube (Section 3), made with mono-energetic neutrons provided by the Filter-Analyzer Neutron Spectrometer (FANS) beamline [9] at the National Institute of Standards and Technology (NIST) Center for Neutron Research (NCNR). The second set of measurements were whole-sensor irradiations, using a moderated ${}^{252}\text{Cf}$ source, which more closely mimic the conditions under which the sensors will operate in space (Section 5).

For all of our measurements, our sensors were paired with a Kromek 550 preamplifier and an Eagle Classic pulse height analyzer (PHA). The PHA provided high voltage (1300 V) bias to the sensors, as well as all signal processing. Pulse-height signals were digitized and recorded in a 256-channel-long spectrum. Shaping times of 8 μs (for ${}^{252}\text{Cf}$ sources) and 6 μs (for FANS measurements) were used. This setup provided an energy resolution of 3.5% for the 764-keV neutron capture peak (e.g. Fig. 1), although we note that the energy resolution degraded to approximately 6% for the FANS measurements due to higher (≈ 5 kHz) rates in the detector.

Our experiments were conducted with five identical sensors. Sensors 1–3 are the engineering model sensors for the Psyche Neutron Spectrometer (NS). Sensors 4 and 5 are the engineering models for the MMX NS. Data from Sensor 5 was used for efficiency measurements but not peak gain measurements, as the GPC exhibited peak broadening attributed to contamination of the ${}^3\text{He}$ gas. Sensor 4 measurements

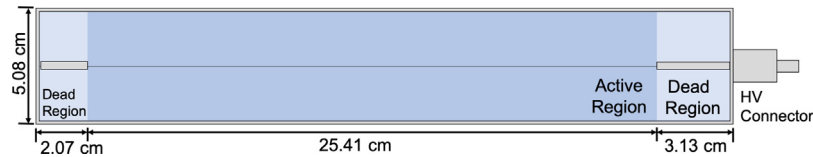


Fig. 2. The dimensions of the ${}^3\text{He}$ GPC sensor used in this study. The sensor has an aluminum housing and 1013 kPa (10 atm) of ${}^3\text{He}$ gas. The housing is 1.4-mm thick on all sides. The interior of the sensor is notional, highlighting the proportional wire and insulators for context only.

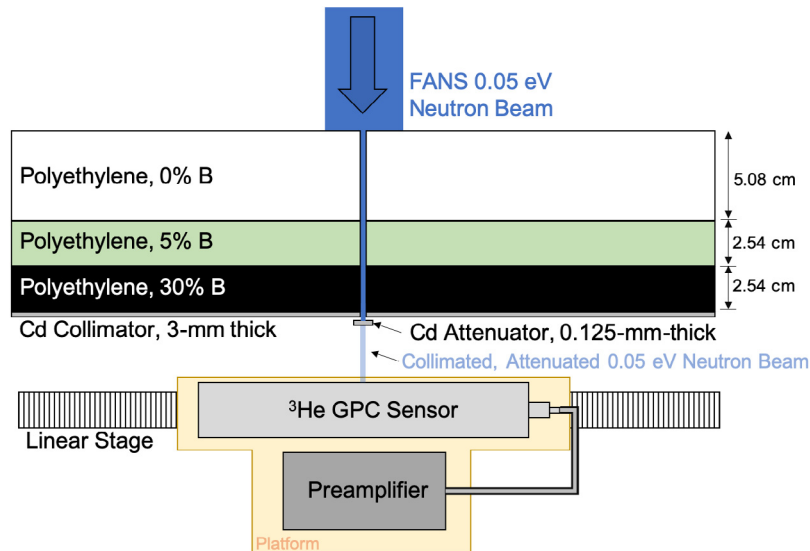


Fig. 3. Diagram of the experiment, including the beam collimation scheme (boron-graded polyethylene shielding and Cd collimator), Cd beam attenuator, sensor placement, and linear stage. Image is not drawn to scale. Note that the preamplifier sits below the platform and is not in the beam path.

are used for peak gain analysis but not efficiency measurements, due to a change in the configuration of the beam collimator during those measurements.

3. Profile efficiency measurements

3.1. Experiment design

We required a highly-collimated neutron beam in order to characterize the position-dependent response along the length of the GPC. This neutron beam was provided by the NCNR FANS facility, which uses a crystalline Cu(220) monochromator to diffract polychromatic neutrons from the 20 MW nuclear reactor to facilitate energy selection via spatial selection. The use of a monoenergetic beam allowed us to isolate position-dependent effects from energy-dependent variations in detection efficiency (see Section 4.2).

A FANS setting of 60.5° provides a 0.05 eV neutron beam to the sample position. 0.05 eV samples the detector response in the regime for which ≈100% neutron detection efficiency is expected within the gas. A 20° collimator upstream of the monochromator limited the neutron flux within FANS, and a low-energy bandpass filter and 10° collimator downstream of the monochromator further reduced the neutron flux at the sample position. The energy spread of this collimated beam was <<0.002 eV.

The 0.05 eV FANS neutron beam, along with an uncollimated fast neutron component from FANS, was further collimated at our experiment with a boron-graded polyethylene shield and a Cd sheet, both having a 3-mm-wide slit (Fig. 3). At the exit of the Cd collimator, a 0.125-mm-thick Cd foil was used to reduce the neutron beam intensity at the detector. This configuration is referred to as the “collimator open” setting. The “collimator closed” setting adds an additional 2-mm-thick Cd sheet in the collimator, eliminating all 0.05 eV neutrons at the sample position. The collimator-closed position facilitated background measurements.

Our ^3He GPC sensor was placed at the FANS sample position on a linear stage whose full translation range allowed the entire length of the GPC to be positioned in the collimated beam over the course of the measurement campaign (Fig. 3). The collimated 0.05-eV neutron beam samples the entire height of the tube (5.08 cm), but only a small fraction of its length (3-mm of 30.6 cm total length).

3.2. Neutron beam characterization

The neutron flux was measured with a fission chamber containing a 595 μg deposit of ^{235}U with an area of 126.7 mm^2 . Neutron-induced fission events in the deposit are detected in an ion chamber and used to determine the deposit-incident neutron flux using the known ^{235}U fission cross section at 0.05 eV and the mass of the deposit. This calculation includes corrections for neutron losses and scattering in the fission chamber housing. Note that the fission chamber is typically used to measure fluxes for neutron beams larger than the ^{235}U deposit. For this analysis, the fission chamber sampled approximately 20% of the full beam height, which we assume was representative of the entire beam height.

A measurement directly upstream of our collimator yielded a neutron flux of $(5.80 \pm 0.17) \times 10^5 \text{ cm}^{-2} \text{ s}^{-1}$. Behind our collimator, approximately 5 cm in front of the GPC, we measured a neutron flux of $(5.50 \pm 0.17) \times 10^3 \text{ cm}^{-2} \text{ s}^{-1}$ for the collimator open configuration. In addition to the normal corrections, this flux calculation included a correction for the fraction of the ^{235}U deposit transected by the collimated neutron beam. This correction factor ($37.74 \text{ mm}^2/126.7 \text{ mm}^2$) assumes the collimated neutron beam is perfectly centered on the deposit. There is an uncharacterized systematic uncertainty associated with this assumption. A prior set of measurements, made in collimator-open and collimator-closed configurations, yielded an estimate of the fraction of the neutron beam having energies above the Cd cutoff (>0.3 eV) to be $7.3 \pm 1.2\%$. We assumed that this ratio was unchanged for our configuration, yielding a neutron flux at the collimator exit of $(5.10 \pm 0.86) \times 10^3 \text{ cm}^{-2} \text{ s}^{-1}$.

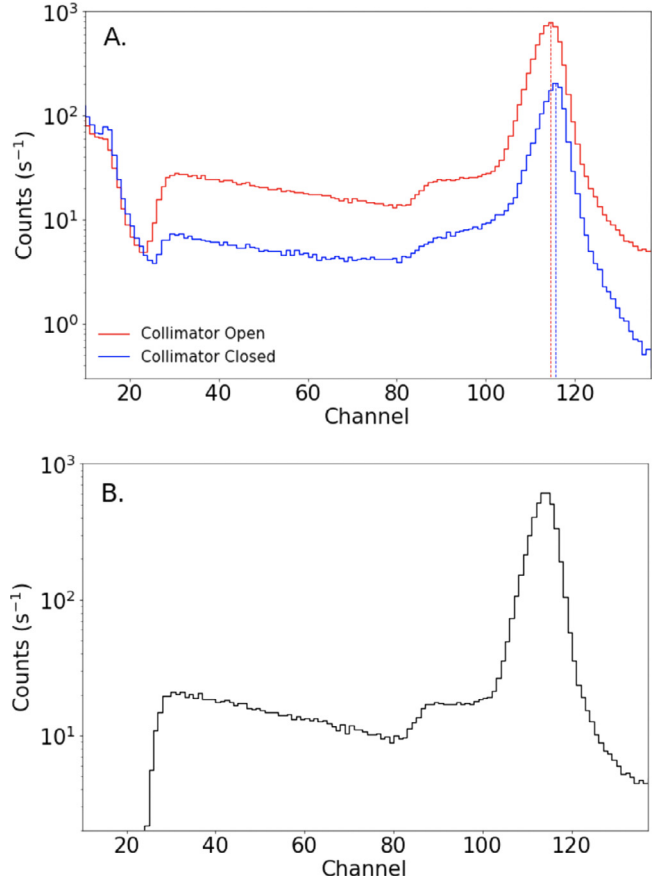


Fig. 4. A. Pulse-height spectrum measurements with the collimator open (e.g. the 0.05 eV beam plus room backgrounds; red) and the collimator closed (e.g. room background only; blue). Dashed lines denote the center of the neutron capture peaks for each measurement. B. The difference spectrum (open–closed data), which we attribute to the signal from the collimated (0.05 eV) neutron component only. (For interpretation of the references to color in this figure legend, the reader is referred to the web version of this article.)

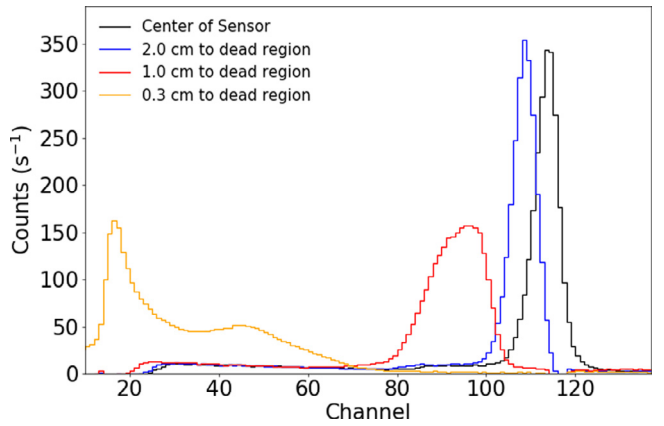


Fig. 5. Neutron capture peak shape for measurements made at four positions along the GPC. The spectra were chosen to highlight the lower peak centroid (gas gain loss) and distorted peak shapes that occur in the “edge effect” region, near the dead regions but still within the active gas volume.

3.3. Measurements

Our graded shield design was effective at blocking both the 0.05-eV beam component and the fast neutron “background” component originating from FANS. However, both beam components travel through

the 3-mm collimator slit to reach the sample position. We remove the fast neutron beam contaminant by performing two measurements at each position along the tube. The first measurement is made with the collimator open (0.125-mm-thick Cd attenuator only). This measurement includes all neutron energies in the FANS beam. The second measurement is performed with the collimator closed (blocked with a total of 2.125 mm of Cd). In this setup, the 0.05 eV beam does not reach the sensor, and the measured rate is due to the higher-energy beam contaminant only. The difference between these two measurements is attributed to the 0.05 eV neutron beam.

Sample spectra from a measurement made at the center of a GPC, with the collimator open and closed, are shown in Fig. 4A. Fig. 4B plots the difference spectrum, which we attribute to the 0.05 eV neutrons only. These data highlight the good signal-to-background, on the order of 5:1 as calculated from the difference spectrum versus the collimator-open spectrum, that we achieved with the collimator and upstream shielding. The data also highlight the slight shift in energy for the beam contaminant (centroid channel is 115.6 for the collimator closed measurement) as compared to the value for the open (signal plus contaminant) measurement (centroid is 114.6) that is diagnostic of higher neutron energies in the beam contaminant.

Translating the linear stage across the collimator line-of-sight allows the response of the entire length of the sensor to be characterized. Spectra from the collimated signal only, achieved following subtraction of the background as measured with the collimator closed, are shown for several different positions along the GPC in Fig. 5. Those data were selected to highlight the edge effect, which manifests as a distorted neutron capture peak whose gain (position) degrades from the full-energy neutron capture peak near the center of the tube to the gain = 1 peak as the neutron beam approaches the dead region.

We quantify the gain of the GPCs versus position by calculating the ratio between the centroids of the neutron-capture peak and the gain = 1 peak. This measured gas gain value is plotted versus position along the sensor in Fig. 6. Loss of gas gain is apparent within the active volume near the boundary with the dead regions. Fig. 6 also plots the neutron capture peak rate, calculated from simple region-of-interest (ROI) summing around the capture peak, as a function of position. The ROI fully encompasses the capture peak for nominal gas gain values, but as the gain decreases near the edge of the active volume, neutron capture events fall outside of the ROI and the result is a decrease in the neutron detection rate.

4. Response modeling

4.1. Gas multiplication modeling

Loss of gas gain had been proposed as an explanation for efficiency loss in GPCs [2,3]; however, to date there has been no effort to develop a quantitative match between gas multiplication models and measurements. Prior analytical modeling of gas multiplication [10–13] assumed an infinitely long tube and ignored the edge effect of the electric field distribution. In order to account for the edge effect, we used finite element analysis to model the electric field distribution, a result that was incorporated into a generic gas multiplication model to predict the location-dependent gas multiplication factor.

The generic expression of the gas multiplication factor (M) is

$$\ln M = - \int_{r_a}^{r_c} \alpha dr, \quad (1)$$

where r_c is the inner radius of the tube, r_a is the radius of the anode wire, and α is the Townsend Coefficient, which is given by [14] as:

$$\alpha = \frac{1}{\lambda} e^{-\frac{W}{E\lambda}}, \quad (2)$$

where λ is the electron mean free path, W is the threshold energy for ionization, and E is the local electric field strength. E can be calculated analytically, when the edge effect is ignored, as:

$$E(r) = \frac{V}{\ln \left(\frac{r_c}{r_a} \right) r}, \quad (3)$$

where V is the anode voltage. For this scenario, the gas multiplication factor is provided by [15] as:

$$\ln M = \frac{V}{A} e^{-\frac{AB}{V}}. \quad (4)$$

The parameters A and B were determined via curve fitting of measured gas multiplication factor versus applied voltage for our sensors (Fig. 7). This fitting yielded values of $A = 50.06$ V and $B = 66.93$.

Our axisymmetric electric field simulation of the GPC was developed using the COMSOL Multiphysics code (Fig. 8). From this simulation, the Townsend Coefficient α was calculated for all points within the tube using our fitted A and B values and the simulated electric field values. Integrating along the radial direction provides the position-dependent distribution of the gas multiplication factor along the length of the GPC, which is plotted in Fig. 6. The agreement between the measurements and the models provide strong evidence for a loss of gas gain at the edges of the active region, where the high-voltage field is modified near the unbiased (dead) volumes of gas at the ends of the sensor. This loss of gas gain explains the distorted peaks shapes (Figs. 5, 6) and loss of neutron detection efficiency (Fig. 6) at the edges of the GPCs. The impact of this loss of gain for the neutron efficiency is discussed further in Section 6.

4.2. Radiation transport modeling

We also used the Geant4 radiation transport toolkit [16–18] to model the GPC profile measurements. Our code, which was developed from the Geant4 example application AnaEx01, tracks neutron capture and reaction product energy loss within the active gas volume. The model uses the QGSP_BIC_HP physics list and G4NDL4.5 neutron cross section library. All recommended options for Geant4 high-precision (HP) neutron physics are set, following the guidelines in the Geant4 Application Developer's Guide, as:

- G4NEUTRONHP_NEGLECT_DOPPLER=1
- G4NEUTRONHP_DO_NOT_ADJUST_FINAL_STATE=1,
- G4NEUTRONHP_SKIP_MISSING_ISOTOPES=1
- AllowForHeavyElements=1

These options lower the computation time for the models without adversely affecting the model output. The range cut for these models was 0.1 mm, a choice that improved the precision of the model at the expense of increased computation time.

The Geant4 detector volumes were defined using dimensions from a mechanical drawing of the ^3He sensor provided by the manufacturer. Pertinent dimensions are shown in Fig. 2. The sensor geometry was composed of four volumes: the aluminum housing, the active gas volume, and the two dead volumes. The active volume, the only volume in which neutron-capture events were recorded, was a 4.8-cm diameter by 25.4-cm-long cylinder of ^3He gas (1013 kPa = 1.35×10^{-3} g cm $^{-3}$). The dead volumes had the same gas composition and diameter, but different lengths (1.93 cm and 2.99 cm). The larger dead volume is closer to the high-voltage connector (Fig. 2). The Al housing was a hollowed cylinder, with 1.4 mm thick walls, that enclosed all other volumes. The “TS Aluminum Metal” composition was used for the aluminum in the housing, as it has the most accurate thermal neutron scattering (TS) cross sections for aluminum that are available for Geant4.

Neutrons were implemented within the model using the General-ParticleSource (GPS) particle generator. The collimated neutron source was defined as a planar beam of 0.05 eV neutrons. For one set of simulations, the beam had the same dimensions (3-mm wide, 50.8-mm tall) as the collimated neutron beam (Section 3.1). For a second set of simulations, the beam size was increased to account for the maximum angular dispersion expected at the GPC. The position of this beam along the GPC was adjusted within the models to replicate the translation of the sensor across the beam (Section 3.3).

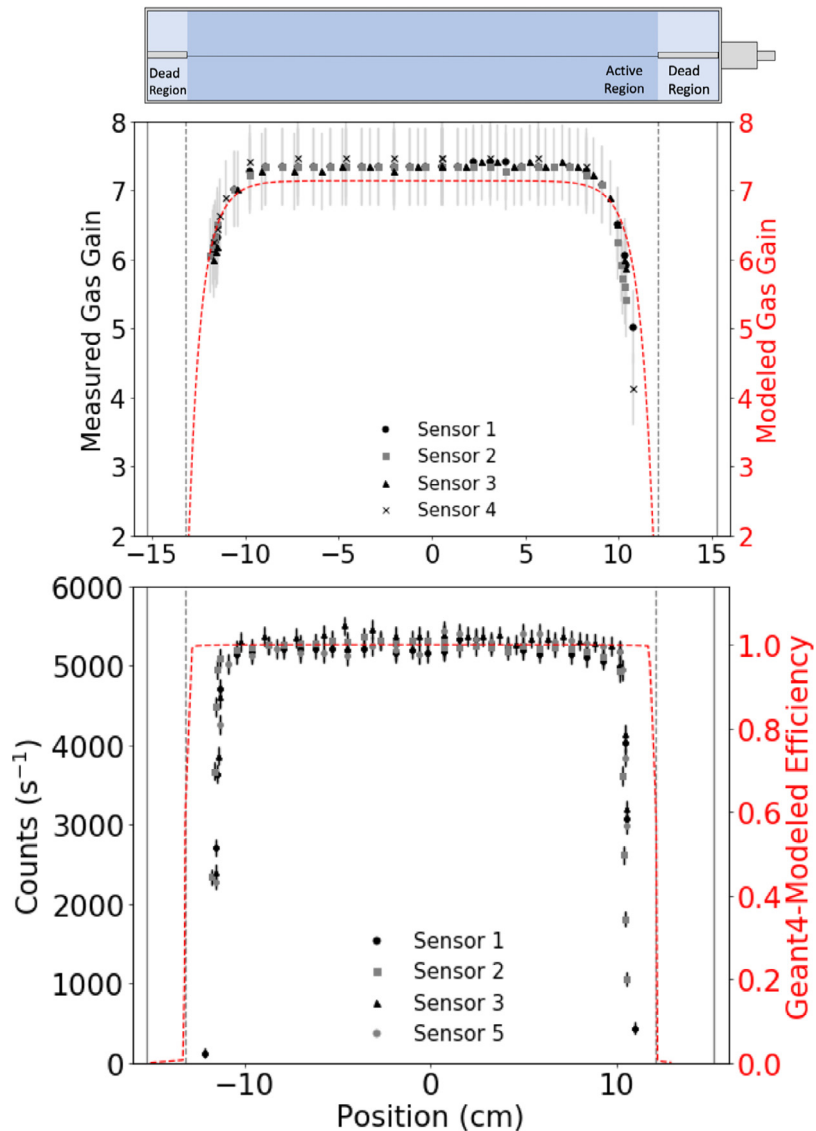


Fig. 6. (Top Panel) The geometry of the ${}^3\text{He}$ GPC sensor used in this study, to scale with the middle and bottom panels. Dark blue is the active gas volume, light blue is the dead regions. (Middle Panel) Measured gas gain values as a function of the position of the collimated (3-mm-wide) neutron beam, for four identical sensors. Modeled gas gain values are shown as the dashed red curve. (Bottom Panel) Measured neutron capture rates, derived from the neutron-capture peak region-of-interest (ROI). The red dashed lines show the Geant4-modeled neutron detection efficiency. For the middle and bottom panels, vertical gray dashed lines represent the boundaries of the dead volumes. (For interpretation of the references to color in this figure legend, the reader is referred to the web version of this article.)

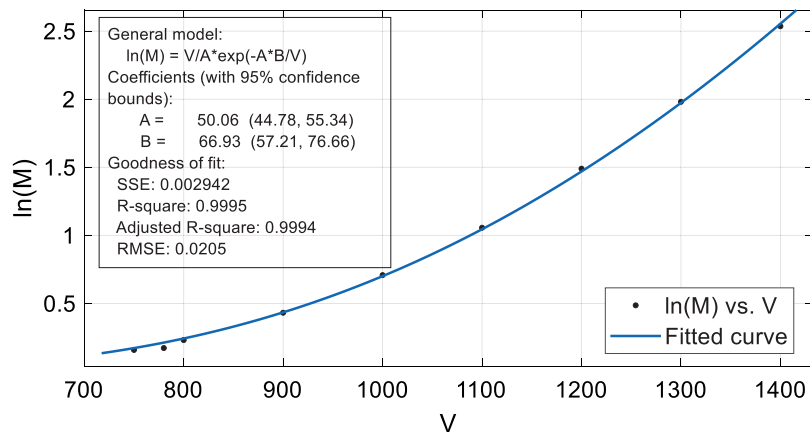


Fig. 7. Derivation of A and B via fitting of measured gain values, $\ln(M)$, as a function of the high-voltage bias applied to the anode (in volts; V).

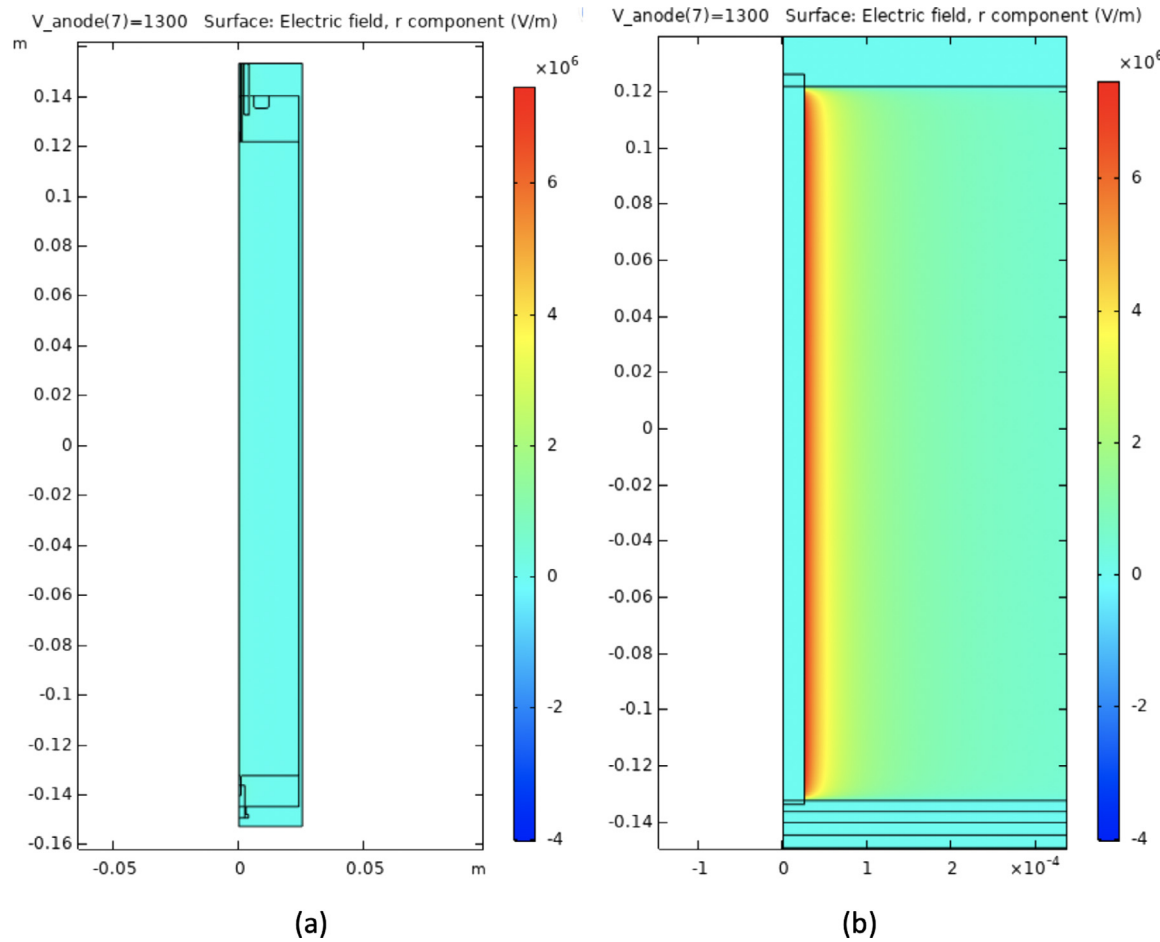


Fig. 8. Axisymmetric electric radial field (V/m) COMSOL simulation for our gas proportional counter and 1300 V bias: (a) full tube, (b) scaled and zoomed in to show the field distribution near the anode.

AnaEx01 natively tracks energy deposition (dE) in active detector volumes. The output is an event-by-event tally of total dE for each history. dE is calculated for all primary and secondary particles interacting in the volume and is dominated by ionization losses from the products of the ${}^3\text{He}(n,p)\text{t}$ reaction. An Interactive Data Language (IDL) script reads the event-by-event dE tally of the simulation and creates a histogram with the same channel size and energy range as the measurements. The output of this model, normalized to the count rate measured at NIST, is shown in Fig. 6 (bottom panel). Note the disagreement between the Geant4 model and measured position-dependent count rates near the ends of the active volume. This contrasts with the gas-gain model (Section 4.1), which provides a qualitative match to the behavior near the dead regions (Fig. 6). In summary, Geant4 radiation transport models typically do not model gas gain, therefore they must be combined with knowledge of edge-effect efficiency loss prior to developing response models like those used for planetary nuclear spectroscopy applications (Section 6).

In addition to modeling the 0.05 eV profile measurements, the Geant4 model was also used to simulate the energy-dependent neutron detection efficiency at the center of the sensor. At this location, the edge

effect is not relevant and the Geant4-modeled efficiency is accurate. The results, shown in Fig. 9, report the neutron detection probability for the NIST experiment geometry. ${}^3\text{He}$ GPCs are generally almost 100% efficient at measuring sensor-incident neutrons with energies below about 0.1 eV, with a rapidly dropping ($\sim 1/v$; where v is the neutron velocity) efficiency extending to a maximum energy of about 1 keV. The $\sim 1/v$ dependence is observed in our model, and our measured efficiency at <0.1 eV is approximately 85%. We propose two explanations for our maximum efficiency being $<100\%$. The first is the difference between the beam and GPC height (5.08 cm) and the height of the active gas volume (4.8 cm), i.e. some neutrons are undetected because they never intersect the active gas volume. The second explanation is that the cylindrical shape of the GPCs provide less neutron-detecting gas at the edges of the sensor, with a corresponding reduction in efficiency at these geometric extremes.

The NIST measurements provide a means of benchmarking our models. The measured neutron capture rate in the center of the GPC, averaged for all sensors and measurements (Fig. 6, bottom), is $(4.4 \pm 0.5) \times 10^3 \text{ cm}^{-2} \text{ s}^{-1}$. Dividing this value by the background-corrected neutron flux measured with the fission chamber of $(5.10 \pm 0.86) \times 10^3 \text{ cm}^{-2} \text{ s}^{-1}$, and adding an extra 20% uncertainty to account for unquantified beam divergence, yields an efficiency of $(81 \pm 21)\%$ (see Fig. 9) for 0.05 eV neutrons incident on the center of the GPC. This value is consistent with the modeled efficiency value (Fig. 9). The extra 20% uncertainty

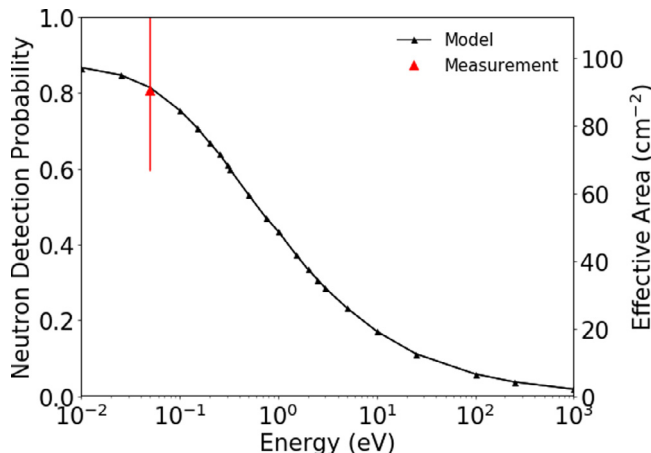


Fig. 9. Geant4-simulated neutron detection efficiency of the GPC for a plane wave of neutrons, incident on the center of the GPC, perpendicular to the long-axis of the GPC, in a 3-mm beam, 5.08-cm tall. The measured value is shown in red. The error bar of the measurement is dominated by systematic uncertainties.

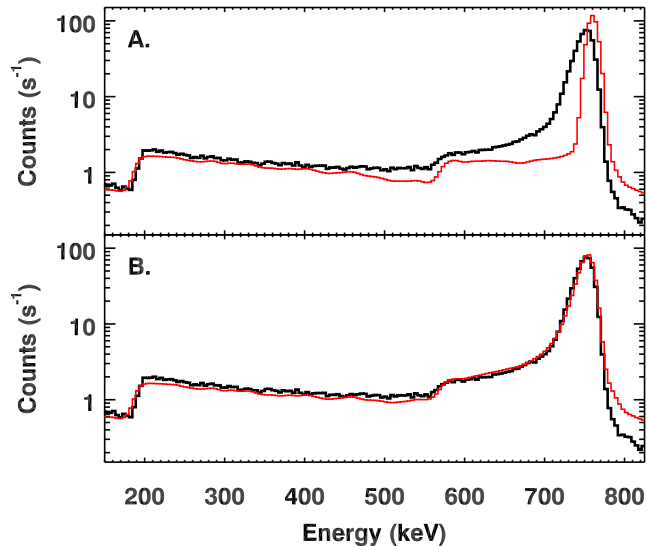


Fig. 10. Comparison of measured (black) and modeled (red) spectra for the whole-tube irradiation with the ²⁵²Cf source. (Top Panel) Simple Gaussian smooth of the model. (Bottom Panel) Two-component smooth, which includes a contribution with an exponentially-modified Gaussian (EMG) shape to approximate contributions from neutron capture events near the dead region (e.g. Fig. 5). (For interpretation of the references to color in this figure legend, the reader is referred to the web version of this article.)

is added to account for the fact that the beam monitor measurement was made approximately 5-cm upstream of the ³He GPC, and that an unquantified beam divergence would reduce the neutron flux at the GPC. The value of 20% captures the maximum beam divergence allowed by our setup.

5. Whole-sensor response measurements

For planetary science applications, the entire volume of the GPC is illuminated with neutrons having a wide range of energies and sensor-incidence angles. We performed a whole-sensor neutron irra-

diation measurement to investigate the impact of the edge effect in this measurement regime. This measurement was carried out with the Psyche engineering model 1 (P1 sensor) and a ²⁵²Cf neutron source. Cf-252 releases neutrons during spontaneous nuclear fission with a mean energy of 2.13 MeV, which is too high for detection in the GPC. A polyethylene moderator reduced the energy of the neutrons to the point where the GPC neutron detection efficiency was higher. The moderator was a hollowed cylinder with 1-cm-thick walls, a length of 24.2 cm, and a mass of 494 g. The moderator was centered on the GPC and enclosed the active volume of the sensor. This geometry produces whole-sensor irradiation with a mixed-energy neutron beam similar to that expected in space.

Our ²⁵²Cf source was placed 30 cm from the center of the tube, a distance chosen to limit the dead time of the measurements to <5%. We collected a 600-s-long measurement of the ²⁵²Cf source irradiation, as well as a 3600-s-long room background run. The background-subtracted ²⁵²Cf source run is shown in Fig. 1. Note the presence of a low-energy tail on the neutron capture peak, which is a manifestation of the edge effect events (e.g. Fig. 5) contributing a fraction of the events in the whole-sensor measurement.

We used the same Geant4 application detailed in Section 4.2 to model this experiment. The only changes were the addition of the polyethylene moderator and the GPS neutron source parameters. The moderator volume was defined as a 24.2-cm-long hollow cylinder with 1-cm-thick walls. The “TS_H_of_Polyethylene” composition for hydrogen was used for the polyethylene, as it has the most accurate thermal neutron scattering (TS) cross sections for hydrogen available for Geant4.

Within GPS, the ²⁵²Cf source was treated as point source emitting neutrons with an isotropic angular distribution. The energy spectrum was adopted from [19]. Cf sources emit neutrons at a rate of 0.1166 s⁻¹ Bq⁻¹ (4316 neutrons s⁻¹ μCi⁻¹; [19]). Our source had an activity of 11.88 MBq (321 μCi), and a corresponding neutron emission rate of 1.39×10⁶ s⁻¹. We simulated 1×10⁹ histories, which is equivalent to 720 s of source-exposure time. An IDL script reads the event-by-event tally output of the Geant4 simulation and creates a histogram with the same channel size and energy range as the measurements. This histogram was divided by the equivalent run time of 720 s to produce a spectrum that is directly comparable to time-normalized measurements.

A direct comparison of the measurement and model requires application of a smooth to approximate the energy resolution of the GPC. Fig. 10 (top) compares the model and measurements following a simple Gaussian smooth of the modeled spectrum. Note that the neutron capture peak tailing we attributed to the edge effect is not reproduced using this simple smoothing routine. This is expected, as Geant4 tracks energy deposition, but not signal multiplication within the gas resulting from the high-voltage bias applied to the sensor. Our Geant4 model has no knowledge of gas gain loss near the edge of the active volume.

To account for the missing edge effect in the model, we performed a separate two-step smooth of the model spectrum. First, 15% of the neutron capture events ($E > 190$ keV) are removed to account for efficiency loss in the edge-effect region. For the remaining events not in the neutron capture peak, the same Gaussian smooth as described above is applied to the data. Within the neutron capture peak, 85% were subjected to the simple Gaussian smooth, and 15% were subjected to an exponentially-modified Gaussian (EMG) smooth with a long tail whose value is empirically derived from the data. The supplemental online material of [20] details the EMG function and its use for fitting nuclear spectroscopy data. These numbers (85% detected; 15% in an exponential tail) were chosen to improve the match between the measurements and the simulation. However, we note that they are similar to our estimate of the efficiency loss due to the edge effect and the fraction of events with reduced gain due to gas gain loss in the edge effect region (Section 6).

This smooth of the model spectrum is compared to the data in Fig. 10 (bottom). Note the substantially improved model-data agreement, which indicates that post-simulation processing of the model can be used to account for the missing edge-effect physics in the Geant4 model. Summing all events in the active-area-corrected model spectra from 180 keV to 800 keV (inclusive of the neutron capture peak and all wall-effect neutrons) yields a modeled counting rate of 755 s^{-1} for the ^{252}Cf neutron source irradiation. The same sum of events in the measured spectrum yields a counting rate of 714 s^{-1} . Our model-to-measured rate is thus 106%, and provides a benchmark of the accuracy of our Geant4 models. We conclude that the models can achieve an accuracy of within 10% of the measured rates when the magnitude of the edge effect is known a priori and applied to the Geant4 output.

6. Discussion

For planetary-science neutron spectroscopy investigations, neutron counting rates are typically derived via summing of spectral regions of interest (ROI) centered on the neutron capture peak, e.g. [21], with corrections made for non-neutron events in the ROI (e.g. cosmic-ray energy deposition in the GPC). This type of analysis is particularly sensitive to signal loss due to the edge effect, as valid neutron-capture events subjected to the edge effect shift to lower pulse height (Fig. 5) and therefore fall outside of the summing ROI. This manifests at neutron detection efficiency loss (Fig. 6, bottom panel).

The count rate profile derived from the ROI summing method (Fig. 6, bottom panel) yields a FWHM active length of $(22.0 \pm 0.6) \text{ cm}$, which is $(87 \pm 2)\%$ of the reported geometric length of the active area (25.41 cm ; Fig. 2). When multiplied by the diameter of the active volume of gas in the GPC (4.8 cm), we calculate an active area of $(106 \pm 3) \text{ cm}^2$, 13% lower than a simple geometric model of the active area ($25.41 \text{ cm} \times 4.8 \text{ cm}$) that does not include the edge effect. Note that this value is specific to our tube geometry and bias voltage and should not be adopted blindly for other ^3He GPC sensors. Edge effect measurements for other ^3He GPCs have also been reported [2,3]. Fig. 9 expands this calculation to include the neutron detection probability versus energy to report the active area of the sensor from 10^{-2} to 10^3 eV , based on the simulated neutron detection probability in the NIST experiment geometry.

The Lunar Prospector (LP) NS data reduction, which used the neutron-capture peak ROI method [20] to determine the neutron flux at the sensor, consistently yielded counting rates that were 10% to 20% lower than corresponding simulated rates [22,23], consistent with our estimate of a 13% efficiency loss for the ROI summing method. The LP NS was a similarly sized GPC with the same ^3He pressure as the GPCs used for this study. We propose that our measurements explain the longstanding discrepancy with the LP NS data.

Edge-effect-induced efficiency loss can be partly mitigated by expanding the summing ROI to limit the number of edge-effect events that fall outside the ROI. Choosing an ROI lower limit just below the lower-energy-edge of the triton wall effect increases efficiency by both including wall effect events and more of the edge-effect events. We note that, for planetary science applications, this alternative approach comes at the cost of increased background contributions from cosmic-ray-induced events. However, use of the wider, wall-effect inclusive ROI allows us to mitigate the efficiency loss problem for the upcoming Psyche, MMX, Dragonfly, and VIPER [24] NS data analyses.

7. Conclusions

Whole-sensor neutron detection efficiency measurements, achieved via irradiation with a moderated ^{252}Cf neutron source, and profile measurements along the length of five separate sensors using a 3-mm-wide, monoenergetic (0.05 eV) neutron beam, allowed us to quantify the active area of a ^3He GPC. We observed that the efficiency-area product (at 0.05 eV) is 13% lower than that expected based solely

on the reported active area of the sensor. The efficiency loss occurs at the ends of the active volumes, adjacent to the non-biased dead volumes. This edge effect has been attributed to a decrease in charge production near the end of the active area, which we confirmed via gas-gain multiplication calculations informed by a finite element model of the position-dependent electrostatic field within our sensor.

Geant4 models of GPC pulse-height spectra require corrections to account for this active area loss. A two-component spectral response smoothing routine of the modeled energy deposition spectrum was required to accurately reproduce the shape and amplitude of the measurements. Following our corrections for the edge-effect efficiency loss, we found that the Geant4 models reproduced the whole-sensor ^{252}Cf -measured count rates to within 10%.

Accurate knowledge of the active area of the neutron sensors studied here is necessary to properly interpret neutron measurements planned for the Psyche and MMX missions to asteroid (16) Psyche [6] and Mars' moon Phobos [7], respectively. The results presented here will be incorporated into analyses of neutron data from those missions. Our Geant4 benchmark provides an estimate of the systematic uncertainties associated with the modeled efficiency measurements (<10%), an uncertainty that will be propagated to all resulted derived from those measurements. Analyses of data from neutron spectrometers on completed (e.g. Lunar Prospector, [21]) and upcoming (e.g. VIPER, [23]; Dragonfly, [8]) missions, which have sensors with different geometries and/or housing materials than the sensors studied here, should conduct similar measurements and modeling efforts to fully understand the active areas prior to interpreting their measurements.

8. Note

Certain commercial equipment, instruments, or materials are identified in this paper in order to specify the experimental procedure adequately. Such identification is not intended to imply recommendation or endorsement by the National Institute of Standards and Technology, nor is it intended to imply that the materials or equipment identified are necessarily the best available for the purpose.

CRediT authorship contribution statement

Patrick N. Peplowski: Conceptualization, Data curation, Formal analysis, Funding acquisition, Investigation, Methodology, Project administration, Software, Supervision, Validation, Visualization, Writing - original draft, Writing - review & editing. **Zachary W. Yokley:** Conceptualization, Investigation, Methodology, Resources, Validation, Visualization, Writing - review & editing. **Madison Liebel:** Data curation, Formal analysis, Investigation, Methodology, Writing - review & editing. **Shuo Cheng:** Formal analysis, Software, Supervision, Visualization, Writing - review & editing. **Richard C. Elphic:** Data curation, Investigation, Writing - review & editing. **Shannon F. Hoogerheide:** Formal analysis, Investigation, Methodology, Writing - review & editing. **David J. Lawrence:** Funding acquisition, Project administration, Resources, Supervision, Writing - review & editing. **Jeffrey S. Nico:** Formal analysis, Investigation, Methodology, Writing - review & editing.

Declaration of competing interest

The authors declare that they have no known competing financial interests or personal relationships that could have appeared to influence the work reported in this paper.

Acknowledgments

This work was funded by NASA's Discovery Program, under the Psyche: Journey to a Metal World mission and the Mars-moon Exploration with GAmma-rays and NEutrons (MEGANE) project. Psyche funding is provided to the Johns Hopkins Applied Physics Laboratory (JHUAPL) through contracts 1569206 from NASA Jet Propulsion Laboratory and 17-256 from Arizona State University. MEGANE funding is provided to JHUAPL directly under contract NNN06AA01C. A portion of this work was supported by the National Institute of Standards and Technology and the NIST Physical Measurement Laboratory. We acknowledge the support of the National Institute of Standards and Technology (NIST), U.S. Department of Commerce, in providing the neutron research facilities used in this work. Specifically, we thank Terrance Udovic, William Ratcliff, and Benjamin Trump of the NIST Center for Neutron Research (NCNR) for assistance planning and executing the tube profile measurements conducted with the FANS instrument. Finally, we thank Erin Hoffer of JHUAPL for help designing some of the support equipment used during the NIST/FANS measurements.

References

- [1] G.F. Knoll, *Radiation Detection and Measurement*, 4th ed., John Wiley & Sons, 2010.
- [2] N. Takeda, K. Kudo, Neutron response functions improved by taking into consideration measured edge effect of ${}^3\text{He}$ proportional counter, *IEEE Trans. Nucl. Sci.* 41 (4) (1994) 880–883.
- [3] K. Kudo, N. Takeda, A. Uritani, S. Koshikawa, Y. Shibata, K. Kobayashi, T. Yoshimoto, Ideal response function of a ${}^3\text{He}$ proportional counter to thermal neutrons determined by different length counters, *Nucl. Instrum. Methods Phys. Res. B* 213 (2004) 305–309.
- [4] W.C. Feldman, K. Ahola, B.L. Barraclough, R.D. Belian, R.K. Black, R.C. Elphic, D.T. Everett, K.R. Fuller, J. Kroesche, D.J. Lawrence, S.L. Lawson, Gamma-ray, neutron, and alpha-particle spectrometers for the Lunar prospector mission, *J. Geophys. Res. Planets* 109 (E7) (2004).
- [5] S. Hahn, R. Elphic, T. Murphy, M. Hodgson, R. Byrd, J. Longmire, D. Lawrence, B. Barraclough, K. Fuller, T. Prettyman, M. Meier, A validation payload for space and atmospheric nuclear event detection, in: 2002 IEEE Nuclear Science Symposium Conference Record, vol. 1, IEEE, 2002, pp. 71–77.
- [6] D.J. Lawrence, M. Burkes, M. Cully, L.T. Elkins-Tanton, J.O. Goldsten, I. Jun, T.J. McCoy, P.N. Peplowski, C.A. Polansky, T.H. Prettyman, B.C. Schratz, K.G. Sukhatme, Z.K. Staniszewski, N.Z. Warner, Z.W. Yokley, The psyche gamma-ray and neutron spectrometer: Update on instrument design and measurement capabilities, in: 50th Lunar and Planetary Science Conference, the Woodlands, TX, 2019, <https://www.hou.usra.edu/meetings/lpsc2019/pdf/1554.pdf>.
- [7] D.J. Lawrence, P.N. Peplowski, A.W. Beck, M.T. Burks, N.L. Chabot, M.J. Cully, R.C. Elphic, C.M. Ernst, S. Fix, J.O. Goldsten, E.M. Hoffer, Measuring the elemental composition of phobos: The mars-moon exploration with gamma rays and neutrons investigation for the martian moons exploration mission, *Earth Space Sci.* (2019).
- [8] Ralph D. Lorenz, Elizabeth P. Turtle, Jason W. Barnes, Melissa G. Trainer, Douglas S. Adams, Kenneth E. Hibbard, Colin Z. Sheldon, Kris. Zachry, Patrick N. Peplowski, David J. Lawrence, Michael A. Ravine, Timothy G. McGee, Kristin S. Sotzen, Shannon M. MacKenzie, Jack W. Langelaan, Sven. Schmitz, Larry S. Wolfarth, Peter D. Bedini, Dragonfly: A Rotorcraft Lander Concept for Scientific Exploration at Titan, Johns Hopkins APL Technical Digest 34 (#3), 2018, pp. 374–387, www.jhuapl.edu/techdigest.
- [9] T.J. Udovic, D.A. Neumann, J. Leao, C.M. Brown, Origin and removal of spurious background peaks in vibrational spectra measured by filter-analyzer neutron spectrometers, *Nucl. Instrum. Methods Phys. Res. A* 517 (1–3) (2004) 189–201.
- [10] W. Diethorn, A methane proportional counter system for natural radiocarbon measurements U.S. Atomic Energy Commission Report NYO-6628, 1956, pp. 69–72.
- [11] R.S. Wolff, Measurement of the gas constants for various proportional-counter gas mixtures, *Nucl. Instrum. Methods* 115 (1974) 461–463.
- [12] A. Zastawny, Gas amplification in a proportional counter with carbon dioxide, *J. Sci. Instrum.* 43 (1966) 179–181.
- [13] J.E. Bateman, A general parametric model for the gain of gas avalanche counters with particular attention to non-cylindrical geometries, *Phys. Rep.* 375 (2003) 411–443.
- [14] J.A. Crowther, *Ions, Electrons and Ionising Radiations*, Edward Arnold, London, 1959.
- [15] J.E. Bateman, A general parametric model for the gain of gas avalanche counters with particular attention to non-cylindrical geometries, *Phys. Rep.* 375 (2003) 411–443.
- [16] S. Agostinelli, J. Allison, K. Amako, J. Apostolakis, H. Araju, P. Arce, M. Asai, D. Axen, S. Banerjee, G. Barrand, F. Behner, L. Bellagamba, J. Boudreau, L. Broglia, A. Brunengo, H. Burkhardt, S. Chauvie, J. Chuma, R. Chytracek, G. Cooperman, G. Cosmo, P. Degtyarenko, A. Dell'Acqua, G. Depaoloa, D. Dietrich, R. Enami, A. Feliciello, C. Ferguson, H. Fessemeldt, G. Folger, F. Foppiano, A. Forti, S. Garelli, S. Giani, R. Giannitrapani, D. Gibin, J.J. Gomez Cadena, I. Gonzalez, G. Gracia Abril, G. Greeniaus, W. Greiner, V. Grichine, A. Grossheim, S. Guatelli, P. Grumlinger, R. Hamatsu, K. Hashimoto, H. Hasui, A. Heikkinen, A. Howard, V. Ivanchenko, A. Johnson, F.W. Jones, J. Kallenbach, N. Kanaya, M. Kawabata, Y. Kawabata, M. Kawaguti, S. Kelner, P. Kent, A. Kimura, T. Kodama, R. Kokoulin, M. Kossov, H. Kurashige, E. Lamanna, T. Lampen, V. Lara, V. Lefebure, F. Lei, M. Liendl, W. Lockman, F. Longo, S. Magni, M. Maire, E. Medernach, K. Minamimoto, P. Mora de Freitas, Y. Morita, K. Murakami, M. Nagamatu, R. Nartallo, P. Nieminen, T. Nishamura, K. Ohtsubo, M. Okamura, S. O'Neale, Y. Oohata, K. Paech, J. Perl, A. Pfeiffer, M.G. Pia, F. Ranjard, A. Rybin, S. Sadilov, E. Di. Salvo, G. Santin, T. Sasaki, N. Savvas, Y. Sawada, S. Scherer, S. Sei, V. Sirotenko, D. Smith, N. Starkov, H. Stoecker, J. Sulik, M. Takahata, S. Tanaka, E. Tcherniaev, E. Safai Tehrani, M. Tropeano, P. Truscott, H. Uno, L. Urban, P. Urban, M. Verderi, A. Walkden, W. Wander, H. Weber, J.P. Wellisch, T. Wenaus, D.C. Williams, D. Wright, T. Yamada, H. Yoshida, D. Zschiesche, GEANT4 – a simulation toolkit, *Nucl. Instrum. Methods A* 506 (2003) 250–303.
- [17] J. Allison, K. Amako, J. Apostolakis, H. Araujo, P. Arce Dubois, M. Asai, G. Barrand, R. Capra, S. Chauvie, R. Chytracek, G.A.P. Cirrone, G. Cooperman, G. Cosmo, G. Cuttone, G.G. Daquino, M. Donszelmann, M. Dressel, G. Folger, F. Foppiano, J. Generowicz, V. Grichine S. Guatelli, P. Gumplinger, A. Heikkinen, I. Hrivnacova, A. Howard, S. Incerti, V. Ivanchenko, T. Johnson, F. Jones, T. Koi, R. Kokoulin, M. Kossov, H. Kurashige, V. Lara, S. Larsson, F. Lei, O. Link, F. Longo, M. Maire, A. Mantero, B. Mascialino, I. McLaren, P. Mendez Lorenzo, K. Minamimoto, K. Murakami, P. Nieminen, L. Pandola, S. Parlati, L. Peralta, J. Perl, A. Pfeiffer, M.G. Pia, A. Ribon, P. Rodrigues, G. Russo, S. Sadilov, G. Santin, T. Sasaki, D. Smith, N. Starkov, S. Tanaka, E. Tcherniaev, B. Tome, A. Trindade, P. Truscott, L. Urban, M. Verderi, A. Walkden, J.P. Wellisch, D.C. Williams, D. Wright, H. Yoshida, Geant4 developments and application, *IEEE Trans. Nucl. Sci.* 53 (1) (2006) 270–278.
- [18] J. Allison, K. Amako, J. Apostolakis, P. Arce, M. Asai, T. Asio, E. Bagli, A. Bagulya, S. Banerjee, G. Barrand, R. Beck, A.G. Bogdanov, D. Brandt, J.M.C. Brown, H. Burkhardt, Ph. Canal, D. Cano-Ott, S. Chauvie, K. Cho, G.A.P. Cirrone, G. Cooperman, M.A. Cortes-Giralo, G. Cosmo, G. Cuttone, G. Depaola, L. Desorgher, X. Dong, A. Dotti, V.D. Elvira, G. Folger, Z. Francis, A. Galoyan, L. Garnier, M. Gayer, K.L. Genser, V.M. Grichine, S. Guatelli, P. Gueye, P. Gumplinger, A.S. Howard, I. Hrivnacova, S. Hwang, S. Incerti, A. Ivanchenko, V.N. Ivanchenko, F.W. Jones, S.Y. Jun, P. Kaitaniemi, N. Karkatsanis, M. Kelsey, A. Kimura, T. Koi, H. Kurashige, A. Lechner, S.B. Lee, Longo, M. Maire, D. Mancusi, A. Mantero, E. Mendoza, B. Morgan, K. Murakami, T. Nikitina, Pandola, P. Paprocki, J. Perl, I. Petrovic, M.G. Pia, W. Pokorski, J.M. Quesada, M. Raine, M.A. Reis, A. Ribon, A. Ristic Fira, F. Romano, G. Russo, G. Santin, T. Sasaki, D. Sawkey, J.I. Shin, I.I. Strakovsky, A. Taborda, S. Tanaka, E. Tcherniaev, B. Tome, T. Toshito, H.N. Tran, P.R. Truscott, L. Urban, V. Uzhinsky, J.M. Verbeke, M. Verderi, B.L. Wendt, H. Wenzel, D.H. Wright, D.M. Wright, T. Yamashia, J. Yarba, H. Yoshida, Recent developments in GEANT4, *Nucl. Instrum. Methods A* 835 (2016) 186–225.
- [19] R. Radev, T. McLean, Neutron Sources for Standard-Based Testing, Lawrence Livermore National Laboratory, LLNL-TR-664160, 2014, <https://e-reports-ext.llnl.gov/pdf/785407.pdf>.
- [20] P.N. Peplowski, L.G. Evans, S.A. Hauck, T.J. McCoy, W.V. Boynton, J.J. Gilliss-Davis, D.S. Ebel, J.O. Goldsten, D.K. Hamara, D.J. Lawrence, R.L. McNutt, Radioactive elements on mercury's surface from MESSENGER: Implications for the planet's formation and evolution, *Science* 333 (6051) (2011) 1850–1852.
- [21] S. Maurice, D.J. Lawrence, W.C. Feldman, R.C. Elphic, O. Gasnault, Reduction of neutron data from lunar prospector, *J. Geophys. Res. Planets* 109 (2004) E7.
- [22] D.J. Lawrence, W.C. Feldman, R.C. Elphic, J.J. Hagerty, S. Maurice, G.W. McKinney, T.H. Prettyman, Improved modeling of lunar prospector neutron spectrometer data: Implications for hydrogen deposits at the lunar poles, *J. Geophys. Res. Planets* 111 (E8) (2006).
- [23] D.J. Lawrence, W.C. Feldman, J.O. Goldsten, T.J. McCoy, D.T. Blewett, W.V. Boynton, L.G. Evans, L.R. Nittler, E.A. Rhodes, S.C. Solomon, Identification and measurement of neutron-absorbing elements on Mercury's surface, *Icarus* 209 (1) (2010) 195–209.
- [24] K. Ennico-Smith, A. Colaprete, R. Elphic, J. Captainm, J. Quinn, K. Zachny, The volatiles investigating polar exploration rover payload, in: 51st Lunar and Planetary Science Conference, the Woodlands, TX, 2020, <https://www.hou.usra.edu/meetings/lpsc2020/pdf/2898.pdf>.